

Design and Optimisation of High-Speed Receivers for 6G Optical Wireless Networks

Elham Sarbazi, Hossein Kazemi, Michael Crisp, Taisir El-Gorashi, Jaafar Elmirghani, Richard Penty, Ian White, Majid Safari and Harald Haas

Abstract

To achieve multi-Gb/s data rates in 6G optical wireless access networks based on narrow infrared (IR) laser beams, a high-speed receiver with two key specifications is needed: a sufficiently large aperture to collect the required optical power and a wide field of view (FOV) to avoid strict alignment issues. This paper puts forward the systematic design and optimisation of multi-tier non-imaging angle diversity receivers (ADRs) composed of compound parabolic concentrators (CPCs) coupled with photodiode (PD) arrays for laser-based optical wireless communication (OWC) links. Design tradeoffs include the gain-FOV tradeoff for each receiver element and the area-bandwidth tradeoff for each PD array. The rate maximisation is formulated as a non-convex optimisation problem under the constraints on the minimum required FOV and the overall ADR dimensions to find optimum configuration of the receiver bandwidth and FOV, and a low-complexity optimal solution is proposed. The ADR performance is studied using computer simulations and insightful design guidelines are provided through various numerical examples. An efficient technique is also proposed to reduce the ADR dimensions based on CPC length truncation. It is shown that a compact ADR with a height of ≤ 0.5 cm and an effective area of ≤ 0.5 cm² reaches a data rate of 12 Gb/s with a half-angle FOV of 30° over a 3 m link distance.

Index Terms

Laser-based optical wireless communication (OWC), angle diversity receiver (ADR), non-imaging optics, rate maximisation, 6G, compact receiver design, vertical cavity surface emitting laser (VCSEL).

This work has been submitted to the IEEE for possible publication. Copyright may be transferred without notice, after which this version may no longer be accessible.

Part of this work has been presented at IEEE Global Communications Conference (GLOBECOM 2022), 4–8 Dec 2022 [1].

I. INTRODUCTION

Sixth generation (6G) wireless networks are envisioned to create an advanced communication infrastructure to support ubiquitous mobile ultra-broadband, ultra-high-speed with low-latency communication, and ultra-high data density services [2]. Optical wireless communication (OWC) based on infrared (IR) laser beams is considered as an enabling technology for 6G with the aim to achieve data rates of multi-Gb/s per user towards the realisation of Terabit/s wireless access networks [3]–[6]. The accomplishment of such an ambitious goal by means of narrow laser beams requires to rethink common approaches used for conventional light fidelity (LiFi) receivers which are primarily tailored to the wide Lambertian emission profile of inexpensive light sources. Such receivers typically use silicon photodiodes (PDs) with an intrinsically wide field of view (FOV) and a relatively large photosensitive area, whose detection bandwidth does not exceed few tens of MHz. Optical wireless receivers consist of an optical concentrator, a photodetector and a transimpedance amplifier (TIA) [7]. Two types of frequently used photodetectors are avalanche photodiodes (APDs) and positive-intrinsic-negative (PIN) diodes. While APDs offer higher sensitivities due to their internal current gain mechanism, PIN diodes have a simpler structure and a much higher bandwidth. Unlike APDs, PIN diodes do not need a high bias voltage to operate, which renders them a more qualified option for integration with battery-operated mobile devices. Though a TIA with a high transimpedance gain is required to amplify the photocurrent generated by a PIN PD to compensate for the lack of internal current gain [8]. Receivers based on APDs operate in shot noise-limited regime, and those using PIN PDs are thermal noise-limited.

An optical concentrator is composed of an imaging or a non-imaging component [9]. Imaging optics is often used to form an image of a light source on the detector plane. Imaging components can be manufactured in compact form and they can provide a diffraction limited spatial resolution. However, they have a limited acceptance angle and hence a very strict requirement for alignment. This necessitates the use of complex alignment systems with prohibitive implementation costs especially for mobile applications [10]–[13]. Another disadvantage of imaging components is that their performance severely degrades with imperfect manufacturing and assembly errors. With non-imaging optics, image formation is not a concern, instead the main purpose is efficient light collection and concentration. Compared to their imaging counterparts, non-imaging components have a wider acceptance angle for a given concentration gain and they are less prone to alignment issues. Also, they are generally larger in size, however, their size can be reduced at the cost of

a slight loss in their concentration performance [14]–[18]. Therefore, non-imaging optics offers more flexibility to meet the design requirements.

The challenges of implementing Gb/s optical wireless receivers for narrow laser beams entail the design of a high-performance optical front-end system for efficient collection and detection of the incident light at high speed. Mobile devices need a compact and low-cost receiver with two key specifications: a large aperture to capture sufficient optical power and a wide FOV to keep connection with the transmitter by eliminating the strict alignment requirement. Designing such a receiver is associated with a twofold challenge. Foremost, there is a tradeoff between the bandwidth and the photosensitive area of a PD. Thus, a high bandwidth comes with a small area, which restricts the collected optical power. The low collection efficiency of a small PD can be compensated by using appropriate light-focusing optics to boost the received signal-to-noise ratio (SNR), in which case a governing tradeoff between the gain and FOV of the optical component comes into play according to the etendue conservation law [14]. Hence, an improved SNR can be obtained in exchange for a reduced FOV and designing a high-speed optical wireless receiver realising a large collecting aperture and a wide FOV at once remains a major challenge.

A. Related Works

To date, several studies in the literature have addressed the existing challenges in the design of high-speed optical wireless receivers and have reported the achieved FOV and data rates through various experimental works. In the following, we review an anthology of closely connected works and identify the remaining issues and research gaps.

In [19], [20], Koonen *et al.* proposed an imaging receiver design based on a Fresnel lens with a large aperture of diameter 50 mm and a full-angle FOV of 10° , whereby they experimentally demonstrated a data rate of 1 Gb/s. In [21], [22], Umezawa *et al.* designed and fabricated an 8×8 array of PIN PDs followed by an aspheric lens of 15 mm in diameter, offering a full-angle FOV of 6° . The authors also reported the achievement of 25 Gb/s transmission over a 10 m link. These studies corroborated that an array of PDs equipped with an optical concentrator can yield an enhanced SNR and a wider FOV compared with a single PD using similar optics.

In [23], Collins *et al.* proposed the use of a fluorescent concentrator made of a quantum dot material for free space optical communications. They showed that such a concentrator can realise an optical gain 50 times higher than an etendue conserving concentrator with the same FOV. In [24], Manousiadis *et al.* demonstrated the performance of a flat fluorescent optical antenna coupled with an APD, attaining a FOV of 60° and an optical gain of 12. In [25], Dong *et al.*

exploited a similar design to achieve the same FOV with an optical gain of 3.2. Although this type of optical receivers are used as a means of circumventing the etendue limitation, they have a low modulation bandwidth of no greater than 50 MHz due to the long fluorescence lifetime. This bandwidth is not adequate for multi-Gb/s receiver design. In addition, fluorescent receivers are only applicable to specific wavelengths in the visible light spectrum. State-of-the-art high-speed receiver designs are discussed as follows.

In [26], [27], Alkhazrag and Ooi *et al.* proposed and demonstrated an imaging receiver structure based on fused fibre-optic tapers (FFOTs), featuring a FOV of 25° and an optical gain of 120. Unlike conventional imaging optics, FFOTs comprise hundreds of thousands of tapered optical fibres and as a result they have larger dimensions and a longer height as compared to the focal length of imaging lenses. On the upside, they can provide ease of alignment. However, the main disadvantage of FFOTs is that they are not widely available and their manufacturing cost is high. In [28], Pham *et al.* designed an imaging receiver with automatic alignment for beam-steered IR light communication links. The proposed receiver is constructed of an imaging lens and a single high-speed photodetector while the whole setup is equipped with a motorised actuator. Although the half-angle FOV is only 0.6° , the actuator automatically adjusts the receiver orientation by using a control algorithm to ensure that the incident light is within the FOV. With this receiver setup, the authors reported data rates of up to 2 Gb/s for a half-power beam diameter of 12 cm. However, such a design involves bulky and costly components which is not suitable for compact and low-cost receiver design purposes.

In [29], Soltani *et al.* proposed a multi-element imaging receiver design based on an *array of arrays* structure for laser-based OWC links. In this structure, each receiver element is composed of a PD array and a commercial aspheric lens by Thorlabs [30], and multiple receiver elements are put together to form the outer array of PD arrays to improve the overall optical gain performance. In order to preserve the receiver bandwidth, each PD is assumed to be followed by a separate TIA of its own and maximal ratio combining (MRC) or threshold-based equal gain combining (EGC) is then applied to process the output signals of individual PDs. The authors formulated an optimisation problem aiming to find the optimum configuration of the proposed structure in terms of the PD side length, the spacing between the PDs in each array and the lens to array distance subject to specific design constraints including the FOV and bit error ratio (BER) requirements. For a minimum required full-angle FOV of 15° and a BER of 10^{-3} , the optimum solution suggests a design with 4 cm^2 total area and a height of 1.8 mm, achieving data rates of 23.8 Gb/s using on-off keying (OOK) modulation and 21.1 Gb/s based on DC biased optical

orthogonal frequency division multiplexing (DCO-OFDM). However, the optimised design uses an aggregate of 64 lenses and over 2300 PDs and TIAs, resulting in a high hardware complexity. Moreover, with the considered lens having a focal length of 820 μm , the receiver performance is optimised within a 43 μm distance from the lens, and as a consequence it is highly sensitive to any displacements in the optical assembly. Any alignment error of a few tens of micrometer degrades the promised FOV as well as the maximum delivered data rate. Such a design is extremely challenging to implement if not impractical, and it comes at a prohibitive fabrication cost.

B. Contributions

Angle diversity receivers (ADRs) are well-known as a promising solution to provide a wide FOV and a high optical gain simultaneously for OWC systems [9], [31], [32]. An ADR design relieves strict alignment requirements and enables connectivity to multiple access points. Besides, the use of ADRs not only improves the mobility performance and allows for a seamless handover, it also addresses the beam obstruction issues. For laser-based OWC systems that demand highly efficient light concentration, a non-imaging receiver design based on compound parabolic concentrators (CPCs) is more appealing as it provides maximum concentration gain determined by the etendue conservation law and more flexibility in the range of acceptance angles.

In this paper, we consider a multi-tier non-imaging ADR architecture based on CPCs where each CPC is coupled with a PD array. After a thorough analytical modelling of the receiver optics and the subsequent signal combining schemes, we present the underlying design tradeoffs that control the receiver bandwidth and FOV. Then, we proceed to rate maximisation problems to find the optimum receiver configuration. Problem formulations are presented under a unified optimisation framework taking into account the FOV constraint as well as additional constraints on the receiver dimensions. To the best of our knowledge, this is the first study that addresses the interplay between the design tradeoffs systematically and deals with the optimisation of the non-imaging ADR configuration for laser-based OWC systems. Furthermore, we put forward a modified ADR design based on truncated CPCs as an efficient approach to attain compact receiver dimensions. The proposed approach is applied to portable devices such as laptops and smart phones in which a confined space is available for 6G receiver integration.

The main contributions of this paper are summarised as follows:

- An in-depth study of the fundamental tradeoffs in high-speed receivers and identifying the interrelated design tradeoffs in a non-imaging ADR.

- Proposing a two-stage signal processing scheme for the multi-element ADR design to reduce the implementation complexity.
- Building a unified and tractable analytical framework for evaluating the receiver performance considering various design parameters. The same framework applies to both short-range and long-range laser-based OWC links regardless of the link distance.
- Formulating and solving non-convex optimisation problems to acquire the optimum ADR configuration under various constraints on its performance and dimensions.
- Providing insightful and detailed discussions on the feasibility and scalability of the receiver design using extensive computer simulation results.
- Proposing an effective modification to downsize the overall ADR dimensions, leading to a low-complexity and compact receiver design for 6G laser-based optical wireless receivers.

The remainder of this paper is organised as follows. In Section II, the beam propagation model and eye safety considerations are introduced. In Section III, details of the receiver architecture and design tradeoffs are presented. In Section IV, the achievable rate analysis and rate maximisation problems are discussed. In Section V, numerical examples with relevant discussions are provided. In Section VI, the modified ADR design and its performance evaluation are presented. Finally, in Section VII, concluding remarks are drawn and future research directions are identified.

II. SYSTEM MODEL

In this study, we consider a single beam optical wireless link with a transmitter composed of a vertical cavity surface emitting laser (VCSEL) followed by a plano-convex lens. The receiver is located at a distance D from the transmitter.

A. Gaussian Beam Propagation

In an optical intensity modulation and direct detection (IM/DD) system, information bits are modulated onto the light intensity. The VCSEL is assumed to have a Gaussian intensity profile. A Gaussian beam is primarily characterised by two parameters: beam waist w_0 and wavelength λ . Assuming the beam is travelling along the z axis, the intensity distribution is given by [33]:

$$I(r, z) = \frac{2P_t}{\pi w^2(z)} \exp\left(-\frac{2r^2}{w^2(z)}\right), \quad (1)$$

where P_t is the transmit optical power, and r and z are the radial and axial positions, respectively. The beam radius $w(z)$ is expressed as [33]:

$$w(z) = w_0 \sqrt{1 + \left(\frac{z}{z_R}\right)^2}. \quad (2)$$

In addition, the Rayleigh range z_R is given by:

$$z_R = \frac{\pi w_0^2 n}{\lambda}, \quad (3)$$

where n represents the refractive index of the medium [33].

In this work, we only need the beam parameters after the lens transformation for the analysis and optimisation of the receiver performance. When refracted by a lens, the incident Gaussian beam is transformed into another Gaussian beam characterised by a different set of parameters: w'_0 , z'_R and $w'(z)$. Details of how these parameters are obtained based on the parameters of a plano-convex lens can be found in [33]. The received optical power of the transformed beam within a circle of radius ρ_0 on the transverse plane at the receiver location (i.e., at $z = D$) is:

$$P_r = P_t \left(1 - \exp\left(-\frac{2\rho_0^2}{(w'(D))^2}\right) \right). \quad (4)$$

B. Eye Safety Considerations

The maximum optical power emitted from a VCSEL is subject to eye safety regulations. The laser safety regulations have been defined by the International electrotechnical commission (IEC) 60825 standard and the American national standards institute (ANSI) [34], [35]. In these standards, the so-called maximum permissible exposure (MPE) is used as a metric for specifying the irradiance limit of a laser source, which must not be exceeded for the corresponding laser class. The MPE value depends on the laser wavelength, the exposure time and the size of the apparent source. The latter is quantified using the subtense angle α which is defined as the plane angle subtended by an apparent source as viewed from a point in space. The subtense angle is a critical parameter for eye safety assessment. It is a measure of the angular extent of the image formed on the retina and indicates how sharply light is focused on the retina. According to [34], if $\alpha < 1.5$ mrad at the measurement distance, the source is classified as a *point source*, otherwise as an *extended source*.

A laser source is considered to be safe, if at any position in space, the fraction of the received power passing through the pupil of the human eye is less than the corresponding MPE value multiplied by the pupil area. Therefore, the laser safety analysis often includes determining the most hazardous position (MHP), which is where the optical power collected by the pupil aperture

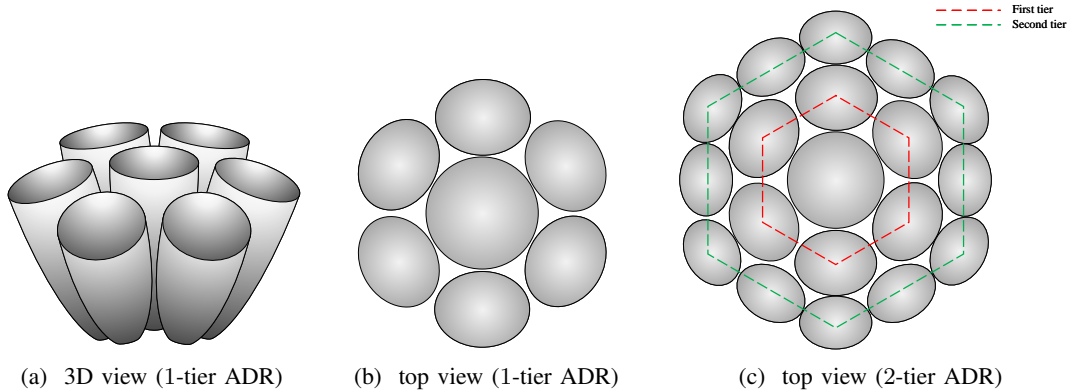


Fig. 1. Angle diversity receiver structure.

is at its maximum. If the eye safety condition is met at this point, it ascertains that anywhere else in space is also eye-safe [36]. In this work, we have taken the eye safety limits into account by closely following the approach presented in [36].

III. HIGH-SPEED RECEIVERS FOR 6G OWC

A. Angle Diversity Receiver

In this study, we consider a non-imaging ADR design by using CPCs. CPCs are non-imaging concentrators that are commonly used in applications requiring efficient light collection. Among various imaging or non-imaging optical components, CPCs can approach the maximum theoretical concentration gain determined by the law of conservation of etendue [14]. In addition, they enable light collection over a relatively wide range of incident angles, thereby providing more flexible designs in terms of the range of acceptance angles as well as alignment tolerances in comparison with imaging optical components such as lenses. Hence, the principal advantage of angle diversity reception based on CPCs is that it allows the receiver to realise a high optical gain and a wide FOV simultaneously.

Figs. 1(a) and 1(b), respectively, illustrate the three-dimensional (3D) structure and the top view of an ADR consisting of seven identical receiver elements oriented in the desired spatial directions. We refer to this design as 1-tier ADR. The overall FOV can be improved by incorporating additional tiers in the ADR structure. To this end, we add tiers according to a hexagonal layout. Let N_{tier} denote the number of tiers. The total number of receiver elements is given by:

$$N_{\text{ADR}} = 1 + \sum_{i=1}^{N_{\text{tier}}} 6i. \quad (5)$$

For instance, Fig. 1(c) shows a 2-tier ADR which consists of $N_{\text{ADR}} = 19$ elements.

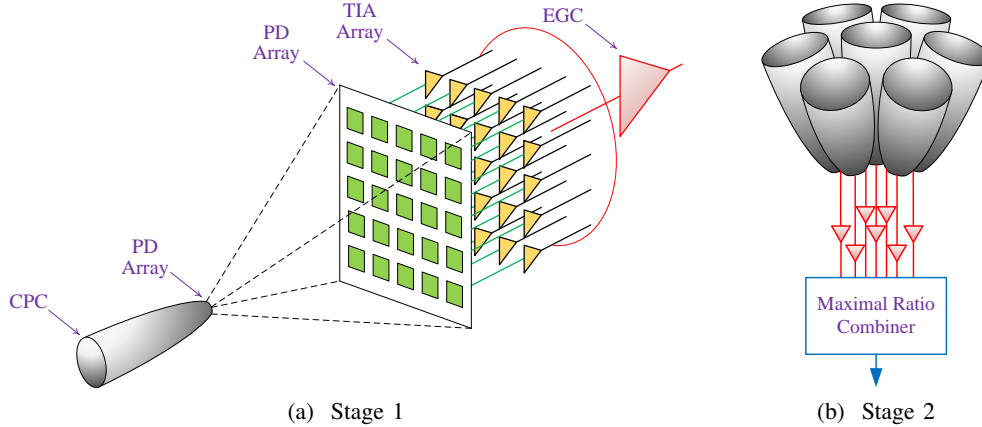


Fig. 2. Two-stage ADR array processing: (a) Stage 1: EGC of the PD array output signals for an ADR element, (b) Stage 2: 7-branch MRC for a 1-tier ADR

Fig. 2(a) depicts the detailed schematic diagram for each ADR element, comprising a CPC paired with a two-dimensional (2D) array of square-shaped PIN PDs. Each PD has a photosensitive area of $A_{PD} = D_{PD}^2$, with D_{PD} denoting the side length of the photosensitive area. The PD array is a square array of size $\sqrt{N_{PD}} \times \sqrt{N_{PD}}$, where N_{PD} is the total number of PDs per array. For a given fill factor (FF) such that $0 < FF \leq 1$, the PD array has a total area of:

$$A = \frac{N_{PD} A_{PD}}{FF}.$$

To avoid compromising the receiver bandwidth, the output signals of the PD array for an ADR element are combined together using EGC by assuming that every PD is independently equipped with a TIA, as shown in Fig. 2(a). Subsequently, the MRC method is employed to combine the output signals of the N_{ADR} elements. This is depicted in Fig. 2(b) for a 1-tier ADR with $N_{ADR} = 7$. The rationale for the proposed two-stage array processing approach is twofold. First, the use of EGC for the PD array aims to maximise the coupling efficiency between the light collection at the entrance aperture and the light detection (i.e., optical-to-electrical conversion) by the PD array at the exit aperture of the CPC under the design considerations. Second, the angular diversity paths are efficiently utilised by applying MRC to the ADR elements to maximise the received SNR. This way the receiver implementation complexity due to the SNR estimation per branch and the computation of MRC coefficients scales with the number of receiver elements, N_{ADR} . Since CPC is an essential constituent of the non-imaging ADR, we briefly describe its working principle and geometry in the following.

Fig. 3 shows the cross section of a CPC. The outer surface of a CPC is a parabolic arc rotated about an axis known as the *CPC axis* or the *rotational axis*. The outer surface is circularly symmetric about the CPC axis with the desired diameter of the entrance aperture, D_1 , at its light

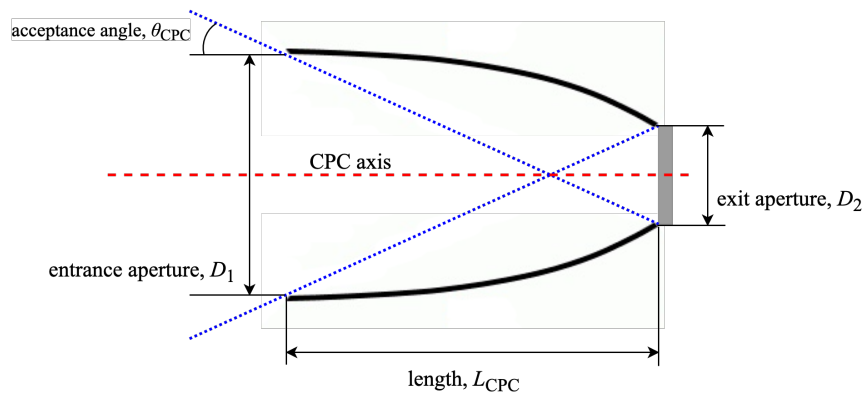


Fig. 3. Cross-section view of a CPC.

collecting end, and the diameter of the exit aperture, D_2 , at its light concentration end. With this geometry, the incident light impinging on the entrance aperture finds its way to the exit aperture via multiple internal reflections, provided it is within the acceptance angle of the CPC, θ_{CPC} . The optical gain is measured by the geometrical concentration ratio, which is defined as the ratio between the areas of the entrance and exit apertures [14], as follows:

$$G_{\text{CPC}} = \left(\frac{D_1}{D_2} \right)^2 = \frac{n_{\text{CPC}}^2}{\sin^2 \theta_{\text{CPC}}}, \quad (6)$$

where n_{CPC} denotes the refractive index of the material used to fabricate the CPC or fill it with. Here, $n_{\text{CPC}} = 1$ for a reflective hollow CPC, and $n_{\text{CPC}} > 1$ for a dielectric CPC. The second equality in (6) represents the maximum theoretical gain for an ideal non-imaging concentrator¹. The overall dimensions of the CPC-based ADR depends primarily on the dimensions of a CPC. This includes the entrance aperture area which is equal to $\pi D_1^2/4$, and the length also referred to as the height of a CPC which is given by [14]:

$$L_{\text{CPC}} = \frac{D_1 + D_2}{2 \tan \theta_{\text{CPC}}}. \quad (7)$$

B. Design Tradeoffs

Designing receivers with the aim of achieving Gb/s data rates presents a twofold challenge: 1) area-bandwidth tradeoff and 2) gain-FOV tradeoff. These tradeoffs are briefly explained in the following.

¹The maximum concentration gain is deduced from the edge-ray principle of non-imaging optics on the basis of the Snell's law and Fermat's principle [14].

1) *Area-Bandwidth Tradeoff*: The bandwidth of a PD is expressed as [7]:

$$B = \frac{1}{\sqrt{(2\pi R_L C_p)^2 + \left(\frac{\ell}{0.44v_s}\right)^2}}, \quad (8)$$

where R_L is junction series resistance plus the load resistance of the TIA, ℓ denotes the thickness of the depletion region, and v_s is the carrier saturation velocity. Also, C_p is the junction capacitance given by $C_p = \frac{\epsilon_0 \epsilon_r A_{PD}}{\ell}$ where ϵ_0 is the permittivity in vacuum, ϵ_r is the relative permittivity of the semiconductor, and A_{PD} denotes the area of the depletion region which constitutes the PD effective area. According to (8), as ℓ decreases, the junction capacitance C_p and therefore the left term in the denominator increases, however, the right term corresponding to the transit time of the PD decreases. Hence, there exists an optimum thickness for the depletion region which yields the maximum PD bandwidth. For this optimum value of ℓ , denoted by ℓ_{opt} , the PD bandwidth is described as [7]:

$$B = \frac{1}{\sqrt{\frac{4\pi\epsilon_0\epsilon_r R_L}{0.44v_s} A_{PD}}}. \quad (9)$$

The area-bandwidth tradeoff for a PD is readily represented by (9). Note that this is in fact an upper bound of the PD bandwidth and any value of $\ell \neq \ell_{opt}$ results in a lower bandwidth. For a square shaped PD with the side length $D_{PD} = \sqrt{A_{PD}}$, (9) turns into:

$$B = \frac{1}{K_{PD} D_{PD}}, \quad (10)$$

where $K_{PD} = \sqrt{\frac{4\pi\epsilon_0\epsilon_r R_L}{0.44v_s}}$. Fig. 4 illustrates the bandwidth B versus D_{PD} for such a PD. This graph is plotted based on (10) using the parameter values adopted from [7]. As shown in Fig. 4, B exhibits a rapidly decreasing behaviour with respect to D_{PD} . Therefore, in order to maximise the PD bandwidth, the junction capacitance has to be minimised. Specifically, for bandwidths higher than 10 GHz, a side length of less than 50 μm is required. This necessitates a very small PD area and imposes a major challenge in the design of laser-based optical wireless receivers, since free-space optical signals need to be collected, aligned with and coupled into the confined photosensitive area of a miniaturised PD with minimal loss.

2) *Gain-FOV Tradeoff*: The small area of a high-bandwidth PD can be compensated by using appropriate imaging or non-imaging optics. This improves the optical power collection efficiency of the optical receiver and thus the received SNR. However, the use of light concentrators for increasing the collection area limits the receiver FOV due to the law of conservation of etendue

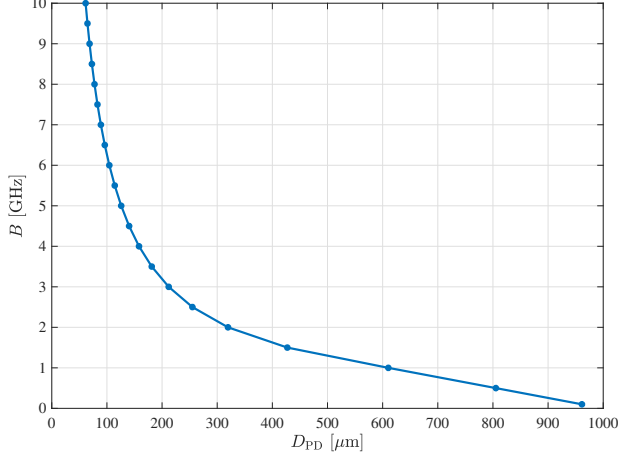


Fig. 4. PD bandwidth versus its side length.

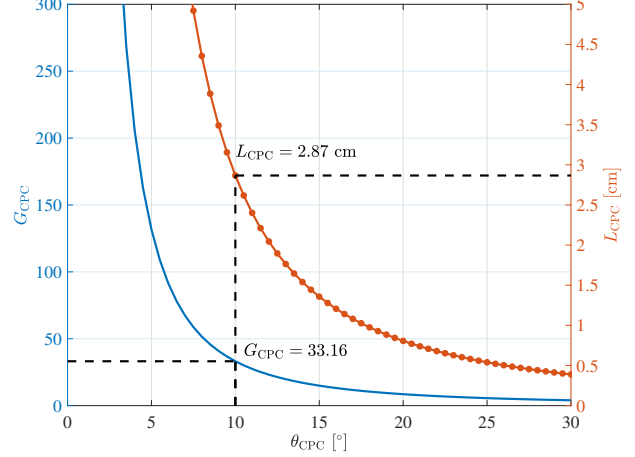


Fig. 5. Gain-FOV tradeoff of a CPC with $n_{\text{CPC}} = 1$ and $D_2 = 1.5$ mm.

[14]. Fig. 5 illustrates the gain-FOV tradeoff for a CPC, where the gain and the length of a CPC with $D_2 = 1.5$ mm are plotted against the acceptance angle, θ_{CPC} . This CPC provides an optical gain of about 33 for $\theta_{\text{CPC}} = 10^\circ$. Such a CPC is 2.87 cm long and it has an effective collection area of about 0.58 cm^2 .

C. Design Parameters

The primary design parameters under consideration are the PD bandwidth B , the half-angle FOV of the ADR, the total number of PDs per array N_{PD} , and the number of ADR tiers N_{tier} . The secondary parameters and how they are related to the primary design parameters are enlisted in the following.

Based on the ADR structure, as shown in Fig. 1, the half-angle FOV is given by:

$$\text{FOV} = \theta_{\text{CPC}} + N_{\text{tier}}\theta_{\text{tilt}}, \quad (11)$$

where θ_{tilt} is the tilt angle between the adjacent ADR tiers. Assuming that the acceptance cones of the adjacent ADR tiers are touching but not overlapping, $\theta_{\text{tilt}} = 2\theta_{\text{CPC}}$. This assumption ensures a full angular acceptance for the ADR design. Therefore, according to (11), the half-angle FOV of the ADR is related to the acceptance angle of CPCs by $\text{FOV} = \theta_{\text{CPC}}(2N_{\text{tier}} + 1)$. Consequently, the secondary parameter θ_{CPC} is expressed in terms of the primary design parameter FOV as:

$$\theta_{\text{CPC}} = \frac{\text{FOV}}{2N_{\text{tier}} + 1}. \quad (12)$$

Noting that the ADR FOV satisfies $\text{FOV} \leq \frac{\pi}{2}$, a useful corollary is deduced from (12).

Corollary 1. For the ADR design with N_{tier} tiers, θ_{CPC} is upper bounded as follows:

$$\theta_{\text{CPC}} \leq \frac{\pi}{6}.$$

The diameter of the exit aperture of the CPC, D_2 , is related to the PD array parameters via:

$$D_2 = D_{\text{PD}} \sqrt{\frac{N_{\text{PD}}}{\text{FF}}}, \quad (13)$$

where FF denotes the PD array FF. From (10), $D_{\text{PD}} = \frac{1}{K_{\text{PD}}B}$. Thus, D_2 can be expressed as:

$$D_2 = \frac{1}{K_{\text{PD}}B} \sqrt{\frac{N_{\text{PD}}}{\text{FF}}}. \quad (14)$$

Based on (6), the diameter of the entrance aperture of the CPC is then given by:

$$D_1 = D_2 \left(\frac{n_{\text{CPC}}}{\sin \theta_{\text{CPC}}} \right) = \frac{1}{K_{\text{PD}}B} \sqrt{\frac{N_{\text{PD}}}{\text{FF}}} \left(\frac{n_{\text{CPC}}}{\sin \theta_{\text{CPC}}} \right). \quad (15)$$

Substituting (14) and (15) into (7) yields:

$$L_{\text{CPC}} = \frac{1}{2K_{\text{PD}}B} \sqrt{\frac{N_{\text{PD}}}{\text{FF}}} \left(\frac{\frac{n_{\text{CPC}}}{\sin \theta_{\text{CPC}}} + 1}{\tan \theta_{\text{CPC}}} \right). \quad (16)$$

The overall size of an ADR with N_{tier} tiers can be described by the length $L_{\text{ADR}} \approx L_{\text{CPC}}$, and the top collection area A_{ADR} . By using (15) and (16), these are derived as:

$$L_{\text{ADR}} \approx \frac{K_1}{B} \left(\frac{n_{\text{CPC}} + \sin \theta_{\text{CPC}}}{\sin \theta_{\text{CPC}} \tan \theta_{\text{CPC}}} \right), \quad (17)$$

$$A_{\text{ADR}} = \frac{\pi D_1^2}{4} \left(1 + \sum_{i=1}^{N_{\text{tier}}} 6i \cos(2i\theta_{\text{CPC}}) \right) = \frac{K_2}{B^2 \sin^2 \theta_{\text{CPC}}} \left(1 + \sum_{i=1}^{N_{\text{tier}}} 6i \cos(2i\theta_{\text{CPC}}) \right), \quad (18)$$

where $K_1 = \frac{1}{2K_{\text{PD}}} \sqrt{\frac{N_{\text{PD}}}{\text{FF}}}$ and $K_2 = \frac{\pi N_{\text{PD}} n_{\text{CPC}}^2}{4\text{FF} K_{\text{PD}}^2}$. Note that the tilt angle of the i th ADR tier relative to the CPC axis of the central ADR element is $\theta_i = i\theta_{\text{tilt}} = 2i\theta_{\text{CPC}}$.

IV. PERFORMANCE ANALYSIS AND OPTIMISATION

For performance analysis, given the triple $(B, \text{FOV}, N_{\text{PD}})$, we first need to determine the ADR dimensions by taking the following steps. We thereupon proceed with performance optimisation.

- 1) For the given FOV, the CPC acceptance angle is obtained from (12).
- 2) For the given B , the corresponding D_{PD} is obtained according to (10).
- 3) The exit and entrance apertures of the CPC are calculated based on (14) and (15).

4) The height L_{ADR} and the overall area A_{ADR} are evaluated based on (17) and (18).

In a fully aligned link, the middle element of the receiver mainly collects the incident optical power. To calculate the received optical power, the effective area of the receiver is approximated by the entrance aperture area of a CPC, within a circle of radius $\frac{D_1}{2}$. The corresponding P_r is thereby calculated based on (4) for $\rho_0 = \frac{D_1}{2}$ in combination with (12) and (15). It follows that:

$$P_r = \text{FF} \times P_t \left(1 - \exp \left(- \frac{N_{\text{PD}} n_{\text{CPC}}^2}{2 \text{FF} \left[K_{\text{PD}} B \sin \left(\frac{\text{FOV}}{2 N_{\text{tier}} + 1} \right) w'(D) \right]^2} \right) \right). \quad (19)$$

To ensure a high spectral efficiency with intensity modulation and direct detection, we assume the use of direct current (DC)-biased optical orthogonal frequency division multiplexing (OFDM) in conjunction with adaptive quadrature amplitude modulation (QAM). By properly choosing the variance of the OFDM signal and the DC bias, the electrical SNR is given by:

$$\text{SNR} = \frac{(R_{\text{PD}} P_r)^2}{\sigma_n^2}, \quad (20)$$

where R_{PD} is the PD responsivity; and $\sigma_n^2 = N_0 B$ is the total noise variance with N_0 denoting the total noise power spectral density (PSD). The total noise PSD is [5]:

$$N_0 = \frac{4\kappa T}{R_L} F_n N_{\text{PD}} + 2q_e R_{\text{PD}} P_r + \text{RIN} (R_{\text{PD}} P_r)^2. \quad (21)$$

In (21), the first term corresponds to the thermal noise, the second term is the shot noise PSD of the receiver, and the third term is the PSD of the relative intensity noise (RIN) of the VCSEL, defined as the mean square of intensity fluctuations of the laser light normalised to the squared average intensity [37]. Also, κ is the Boltzmann constant; T is temperature in Kelvin; R_L is the load resistance; F_n is the noise figure of the TIA; and q_e is the elementary charge. The proposed receiver architecture entails using PD-TIA pairs, as shown in Fig. 2(a). In this case, the total noise is essentially dominated by the receiver thermal noise [5]. Therefore, (21) can be approximated by $N_0 \approx \frac{4\kappa T}{R_L} F_n N_{\text{PD}}$. The achievable rate is given by:

$$R = B \log_2 \left(1 + \frac{\text{SNR}}{\Gamma} \right) = B \log_2 \left(1 + \frac{(R_{\text{PD}} P_r)^2}{\Gamma N_0 B} \right), \quad (22)$$

where B is the single-sided bandwidth of the OWC system which is determined by the receiver

bandwidth²; and Γ denotes the SNR gap required to guarantee the target BER performance.

A. Rate Maximisation

We now formulate an optimisation problem to maximise the achievable data rate for a *given* PD array size N_{PD} and ADR size N_{ADR} . The aim of this optimisation is to find optimum values of B and FOV while satisfying a number of design constraints.

1) *With FOV constraint:* Consider the case where the only constraint in place is the minimum FOV requirement. In this case, the rate maximisation problem can be stated as:

$$\arg \max_{(B, \text{FOV})} R = B \log_2 \left(1 + \frac{(R_{\text{PD}} P_r)^2}{\Gamma N_0 B} \right) \quad (23a)$$

$$\text{s.t.} \quad \text{FOV} \geq \text{FOV}_{\min} \quad (23b)$$

where P_r is given by (19) which is a function of B and FOV. Due to the non-convexity of (23a) in (B, FOV) , this is a non-convex optimisation problem. Let the objective function be denoted by $R = f(B, \text{FOV})$ for brevity. The following proposition brings out a key characteristic of R .

Proposition 1. *R is a monotonically decreasing function of FOV.*

Proof. See Appendix A. ■

The following lemma establishes a key result that is used to simplify the non-convex optimisation problem in (23).

Lemma 1. *The solution to the rate maximisation problem in (23) lies at the boundary of the feasible region.*

Proof. From Proposition 1, it can be concluded that for any given value of $B = B_0$, the objective function $R = f(B_0, \text{FOV})$ under $\text{FOV} \geq \text{FOV}_{\min}$ takes its maximum value at (B_0, FOV_{\min}) . Therefore, R is always maximised at the boundary for $\text{FOV} = \text{FOV}_{\min}$. ■

Theorem 1. *The optimisation problem in (23) is simplified to an unconstrained single variable optimisation problem:*

$$\arg \max_B R = f(B, \text{FOV}_{\min}). \quad (24)$$

Proof. It readily follows from Lemma 1 that (23) for $\text{FOV} = \text{FOV}_{\min}$ reduces to (24). ■

²Here, the system bandwidth is assumed to be limited by the receiver as typically a large modulation bandwidth is available at the VCSEL-based transmitter.

Although the optimisation problem of (24) is still non-convex, its solution can be numerically computed using a one-dimensional search over the range of interest for B .

2) *With FOV and overall dimensions constraint:* When there are additional constraints on the physical dimensions of the ADR as well as the FOV constraint, the rate maximisation problem is formulated as:

$$\arg \max_{(B, \text{FOV})} R = f(B, \text{FOV}) \quad (25a)$$

$$\text{s.t.} \quad \text{FOV} \geq \text{FOV}_{\min} \quad (25b)$$

$$L_{\text{ADR}} \leq L_{\max} \quad (25c)$$

$$A_{\text{ADR}} \leq A_{\max} \quad (25d)$$

The second and the third constraints of (25) are intended to fulfil the design objectives for the top area and the overall height of the ADR. The objective function in (25a) and the two constraints in (25c) and (25d) are all non-convex. As a result, the optimisation problem in (25) is non-convex. By substituting (17) in (25c) and (18) in (25d), both with equality, the optimisation variable B is separately derived as an explicit function of FOV as follows:

$$B = f_L(\text{FOV}) = \frac{K_1}{L_{\max}} \left[\frac{n_{\text{CPC}} + \sin\left(\frac{\text{FOV}}{2N_{\text{tier}} + 1}\right)}{\sin\left(\frac{\text{FOV}}{2N_{\text{tier}} + 1}\right) \tan\left(\frac{\text{FOV}}{2N_{\text{tier}} + 1}\right)} \right], \quad (26)$$

$$B = f_A(\text{FOV}) = \frac{1}{\sin\left(\frac{\text{FOV}}{2N_{\text{tier}} + 1}\right)} \sqrt{\frac{K_2}{A_{\max}} \left[1 + \sum_{i=1}^{N_{\text{tier}}} 6i \cos\left(\frac{2\text{FOV}}{2N_{\text{tier}} + 1}\right) \right]}. \quad (27)$$

Note that (26) and (27) represent boundaries of the two constraints on L_{ADR} and A_{ADR} .

Proposition 2. L_{ADR} and A_{ADR} are monotonically decreasing functions of B and FOV.

Proof. See Appendix B. ■

The following lemma aims to unify the three constraints in (25b)–(25d) based on Proposition 2.

Lemma 2. *The optimisation problem in (25) can be reformulated with a single FOV constraint:*

$$\arg \max_{(B, \text{FOV})} R = f(B, \text{FOV}) \quad (28a)$$

$$\text{s.t.} \quad \text{FOV} \geq f_{\text{FOV}}(B) \quad (28b)$$

with the boundary function $f_{\text{FOV}}(B) = \max \{ \text{FOV}_{\min}, f_L^{-1}(B), f_A^{-1}(B) \}$, where $f_L^{-1}(B)$ and $f_A^{-1}(B)$ are the inverse functions of $B = f_L(\text{FOV})$ and $B = f_A(\text{FOV})$ given in (26) and (27).

Proof. Based on Proposition 2, the dimensions constraints in (25c) and (25d) can be transformed into their equivalent FOV constraints. By defining:

$$\mathcal{S}_1 = \left\{ (B, \text{FOV}) \mid \text{FOV} \geq \text{FOV}_{\min} \right\}, \quad (29a)$$

$$\mathcal{S}_2 = \left\{ (B, \text{FOV}) \mid L_{\text{ADR}}(B, \text{FOV}) \leq L_{\max} \right\} = \left\{ (B, \text{FOV}) \mid \text{FOV} \geq f_L^{-1}(B) \right\}, \quad (29b)$$

$$\mathcal{S}_3 = \left\{ (B, \text{FOV}) \mid A_{\text{ADR}}(B, \text{FOV}) \leq A_{\max} \right\} = \left\{ (B, \text{FOV}) \mid \text{FOV} \geq f_A^{-1}(B) \right\}, \quad (29c)$$

the feasible set of the optimisation problem in (25) takes the following form:

$$\mathcal{S} = \mathcal{S}_1 \cap \mathcal{S}_2 \cap \mathcal{S}_3 = \left\{ (B, \text{FOV}) \mid \text{FOV} \geq \max \{ \text{FOV}_{\min}, f_L^{-1}(B), f_A^{-1}(B) \} \right\}. \quad (30)$$

The boundary of \mathcal{S} as a function of B is:

$$f_{\text{FOV}}(B) = \max \{ \text{FOV}_{\min}, f_L^{-1}(B), f_A^{-1}(B) \}. \quad (31)$$

This completes the proof. ■

The following lemma offers further simplification for the optimisation problem in (28).

Lemma 3. *The solution to the rate maximisation problem in (28) lies at the boundary of the feasible region.*

Proof. Since $R = f(B, \text{FOV})$ is a decreasing function of FOV as shown in Proposition 1, for any given value of $B = B_0$, $R = f(B_0, \text{FOV})$ under $\text{FOV} \geq f_{\text{FOV}}(B_0)$ is maximised at $(B_0, f_{\text{FOV}}(B_0))$. Hence, the maximum of R is located at the boundary of the feasible region. ■

Theorem 2. *The optimisation problem in (28) is simplified to an unconstrained single variable optimisation problem:*

$$\arg \max_B R = f(B, f_{\text{FOV}}(B)) \quad (32)$$

Proof. With the aid of Lemma 3, it suffices to evaluate (28) for $\text{FOV} = f_{\text{FOV}}(B)$. ■

TABLE I
SIMULATION PARAMETERS

Parameter	Description	Value
D	Link distance	3 m
w_0	Incident beam waist radius	10 μm
λ	Laser wavelength	950 nm
P_t	Optical power of the VCSEL	10 mW
n_{CPC}	CPC refractive index	1.7
R_{PD}	PD responsivity	0.6 A/W
F_n	TIA noise figure	5 dB
Γ	SNR gap	2.6
BER	Bit error ratio	3.8×10^{-3}

TABLE II
ADR CONFIGURATIONS

	Configuration	N_{tier}	N_{ADR}	PD Array Size	Total PDs
Single-Tier	Config. 1	1	7	2×2	28
	Config. 2	1	7	4×4	112
	Config. 3	1	7	8×8	448
Multi-Tier	Config. 4	2	19	2×2	76
	Config. 5	2	19	4×4	304
	Config. 6	3	37	2×2	148

The solution to the non-convex optimisation problem in (32) can be efficiently computed using numerical methods by way of a one-dimensional search along the B axis.

V. NUMERICAL RESULTS AND DISCUSSIONS

This section provides numerical results for the narrow-beam OWC link configuration described in Section III. The transmitter is composed of a single VCSEL followed by a plano-convex lens of focal length $f = 33$ mm. The transmitter design is adopted from [5]. For eye safety assessment, the MHP is specified as 10 cm and the maximum permissible optical power of the VCSEL is calculated as $P_{t,\text{max}} = 16$ mW [36]. Here, we assume $P_t = 10$ mW, which satisfies the eye safety condition. The VCSEL-based transmitter provides a Gaussian beam spot of diameter 20 cm at the receiver, which is located at distance $D = 3$ m from the transmitter. Also, without loss of generality, we assume the use of dielectric CPCs, since the optical gain of a dielectric CPC is improved by a factor of n_{CPC}^2 compared to a reflective hollow CPC based on (6). Moreover, $\text{FF} = 0.7$ for each PD array. The rest of the simulation parameters are listed in Table I. In order to evaluate the receiver design, we use various ADR configurations with different number of tiers and PD array sizes, as introduced in Table II. For each configuration, the total number of PDs is calculated as $N_{\text{ADR}} \times N_{\text{PD}}$.

A. Achievable Data Rate and Overall ADR Dimensions

Fig. 6(a)–6(c) illustrate 3D surface plots of the achievable data rate R , the total effective area A_{ADR} and the overall height of the receiver L_{ADR} , respectively, as a function of B and FOV for a 1-tier ADR with Config. 2, which uses 4×4 PD arrays (i.e., $N_{\text{PD}} = 16$). The results are obtained by evaluating R , L_{ADR} and A_{ADR} based on (22), (17) and (18), as per the four-step procedure laid out in Section IV. To interpret the information contained in these 3D

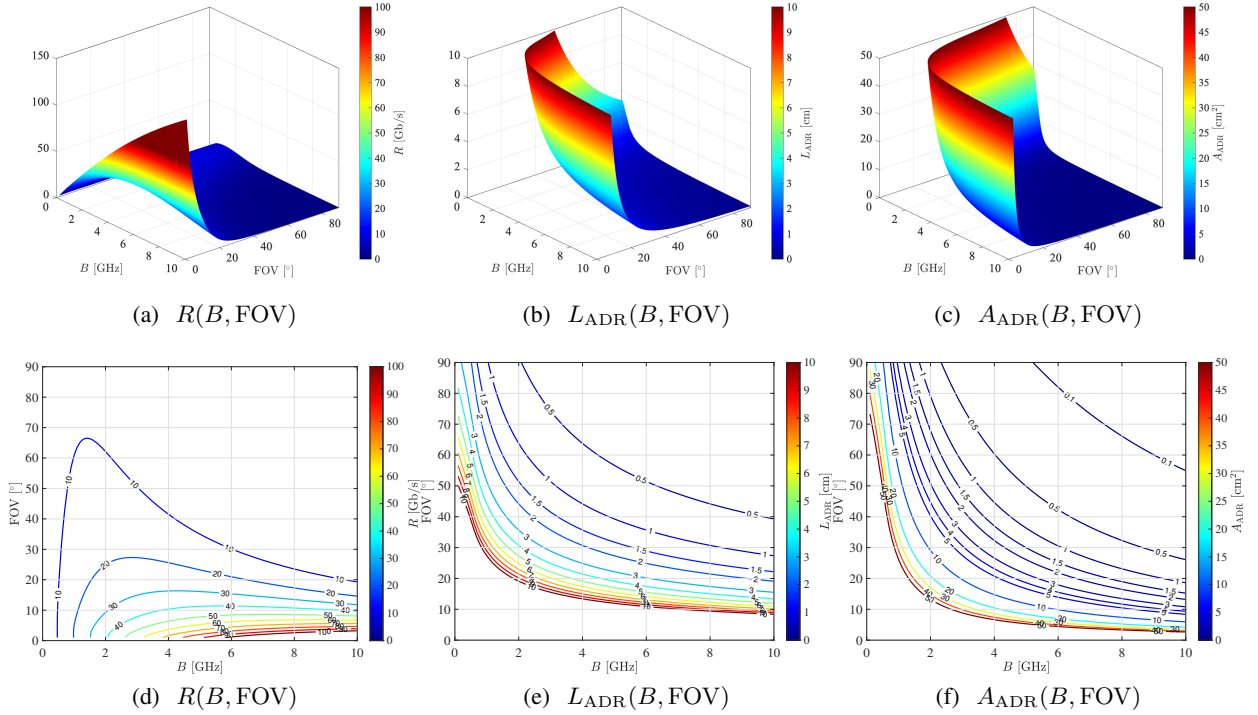


Fig. 6. The achievable data rate R , the overall height L_{ADR} and the total effective area A_{ADR} as a function of the bandwidth B and FOV for Config. 2: (a)–(c) surface plots, (d)–(f) contour plots.

surfaces, the corresponding contour plots³ are presented in Fig. 6(d)–6(f). From Fig. 6(d), it can be observed how the achievable data rate evolves, indicating the point that attaining higher data rates necessitates lower FOVs, which in fact underlines a tradeoff between the achievable rate and FOV. For example, at $R = 10$ Gb/s, $\text{FOV} \leq 65^\circ$ is realisable, whereas when $R = 20$ Gb/s, the resultant FOV is no greater than 28° . By comparison, the constant-height contours specify regions towards the top-right corner of the B -FOV plane where L_{ADR} is less than the given values, as shown in Fig. 6(e). The constant-area contours follow a similar trend, as shown in Fig. 6(f). Comparing this trend with that in Fig. 6(d) reveals another tradeoff between scaling down the receiver dimensions and pushing up the achievable data rate. This tradeoff is elucidated via the following discussion on the rate maximisation under joint FOV and dimensions constraints.

Another perspective to look at the results in Figs. 6(a)–6(c) is through vertical cross sections of the surface plots for a fixed value of FOV. In Fig. 7, R , L_{ADR} and A_{ADR} are plotted against B for $\text{FOV} = 30^\circ$, based on ADR Configs. 1, 2 and 3 with 2×2 , 4×4 and 8×8 PD arrays (i.e., $N_{\text{PD}} = 4, 16, 64$). From Fig. 7(a), it can be seen that for each array size, the achievable

³A contour plot is a graphical representation of a 3D surface on a 2D plane. To clarify, consider a dependent variable Z as a function of two independent variables X and Y . A contour line on the X - Y plane interconnects all the (X, Y) coordinates corresponding to the same value of Z . Alternatively, contour lines can be viewed as intersections of the 3D surface with planes parallel to the X - Y plane for different values of Z , which are projected onto the X - Y plane.

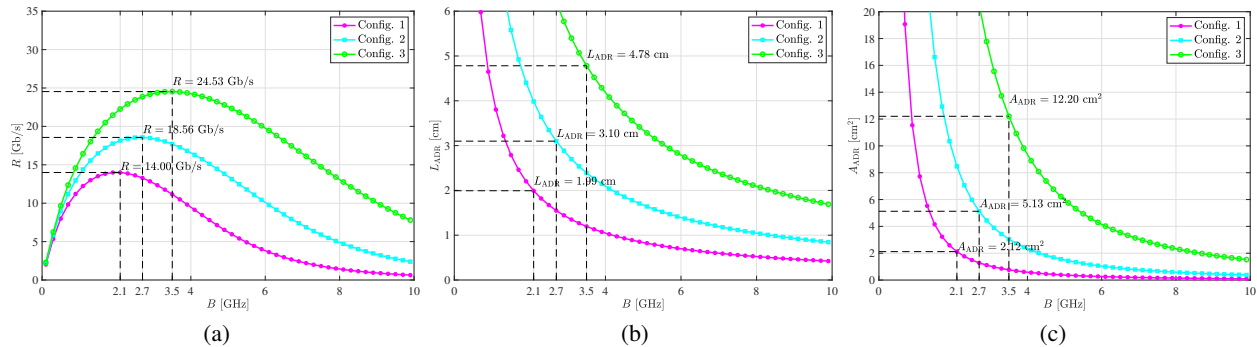


Fig. 7. The achievable data rate R , the overall height L_{ADR} and the total effective area A_{ADR} as a function of the bandwidth B for FOV = 30° for Configs. 1, 2 and 3 based on 2×2 , 4×4 and 8×8 PD arrays, respectively.

data rate has a peak in $2 < B < 4$ GHz; occurring at $B = 2.1, 2.7, 3.5$ GHz for Configs. 1, 2 and 3, respectively. Increasing the bandwidth beyond these values does not help to improve the achievable data rate, but rather brings about a performance degradation. This phenomenon happens as a result of the underlying tradeoffs governing the ADR design. For a given FOV, the optical gain of CPCs and hence the ratio between the entrance and exit aperture areas is fixed in line with the gain-FOV tradeoff. The bandwidth is increased by reducing the PD area according to the area-bandwidth tradeoff, which in turn lessens the total collection area of the PD array for a given array size. Consequently, there is a threshold at which the loss in the power collection efficiency starts to compromise the advantage of a higher bandwidth. Furthermore, it can be observed that the data rate requirement of $R \geq 10$ Gb/s is met by using a 2×2 array. The PD array size can be increased as a means to improve the overall rate performance, as shown in Fig. 7(a), at the expense of enlarging the overall height of the receiver as well as the total effective area, as shown in Figs. 7(b) and 7(c). The triple $(R, L_{\text{ADR}}, A_{\text{ADR}}) = (14.00 \text{ Gb/s}, 1.99 \text{ cm}, 2.12 \text{ cm}^2)$ corresponds to Config. 1 at $B = 2.1$ GHz, which is the best operating point for this configuration in terms of the data rate performance. In this case, it turns out that Config. 1 offers the appropriate ADR design taking account of the hardware complexity, as it uses 4 PDs per receiver element.

B. Design Spaces with Rate and FOV Requirements: Single-Tier ADR vs. Multi-Tier ADR

Fig. 8 illustrates the contour plots of the achievable data rate R . Figs. 8(a)–8(c) correspond to three 1-tier ADR designs composed of 7 CPCs in conjunction with 2×2 , 4×4 , and 8×8 PD arrays, respectively (i.e., $N_{\text{PD}} = 4, 16, 64$). Comparing Configs. 1, 2 and 3 confirms that a larger PD array size leads to a higher overall rate performance. To exemplify the rate maximisation under a minimum FOV constraint only according to the optimisation problem in (23), suppose a FOV $\geq 30^\circ$ is required. The contour plots in Fig. 8 show that the achievable rate is maximised at the point where its curve is tangent to the line FOV = 30°, as indicated by dashed black curves.

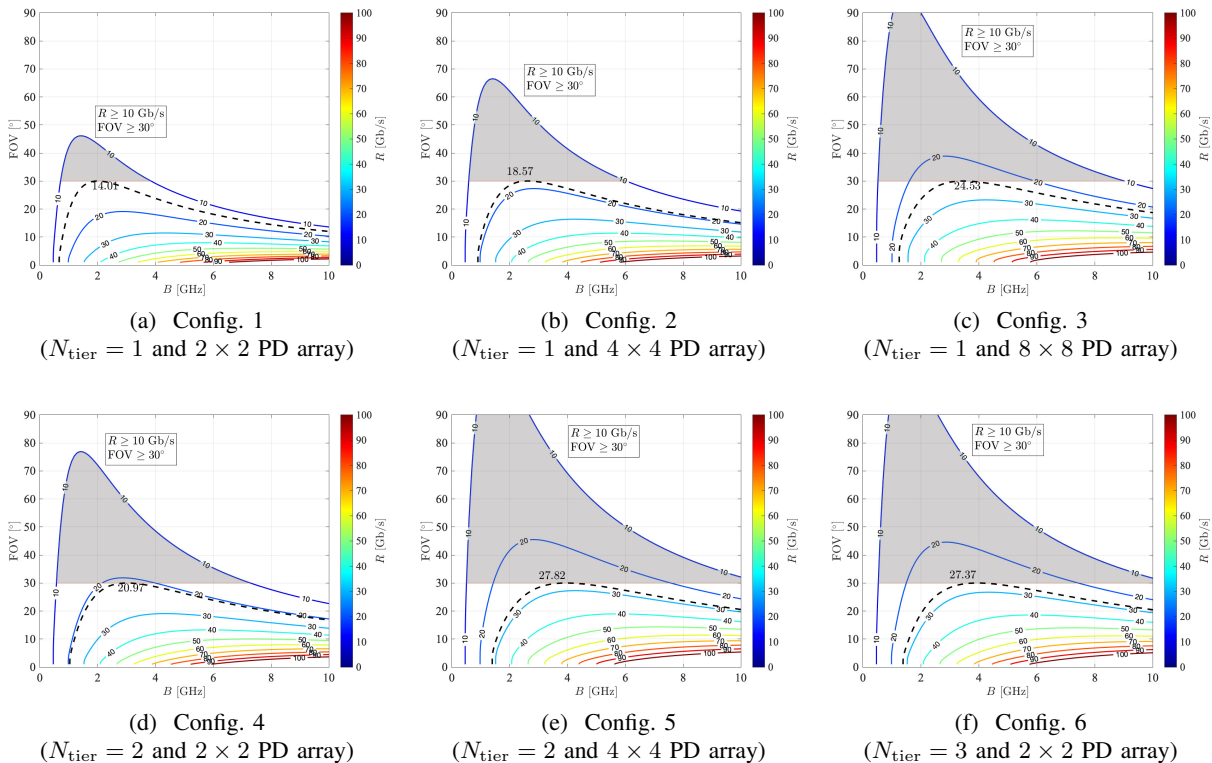


Fig. 8. Contour plots of the achievable data rate R as a function of the bandwidth B and FOV for Configs. 1–6.

The number displayed next to each one represents the maximum value of R for $\text{FOV} \geq 30^\circ$. It can be observed that the maximum data rate of the 1-tier ADR design reaches values greater than 10 Gb/s by means of 2×2 , 4×4 and 8×8 PD arrays, respectively. There are three different multi-tier ADR configurations labelled as Configs. 4, 5 and 6 in Table II. Configs. 4 and 5 are 2-tier ADRs with 76 and 304 PDs in total, respectively, while Config. 6 is a 3-tier ADR having 148 PDs. The contour plots of R for these ADRs are shown and compared in Fig. 8. Config. 3, which is a 1-tier ADR with 448 PDs, is also included as a benchmark for comparison. Suppose the design requirements are $R \geq 10$ Gb/s and $\text{FOV} \geq 30^\circ$, in line with the desired specifications for 6G optical wireless networks [5]. These inequalities jointly define a design space on the B -FOV plane as highlighted in a grey shade in Fig. 8. The design space brings forth the flexibility to choose the PD array parameters while fulfilling the design objectives.

Comparing 2-tier ADR Configs. 4 and 5, as shown in Figs. 8(d) and 8(e), it can be observed that for the same number of tiers, the design space expands when the PD array size and hence the total number of PDs used for each receiver element increases. Besides, comparing 1-tier ADR Config. 3 in Fig. 8(c) with 2-tier ADR Config. 5 in Fig. 8(e) points out that the incorporation of an additional tier results in a larger design space, although a smaller PD array size is used in Config. 5. This is also evident when moving on to 3-tier ADR Config. 6, as shown in Fig. 8(f).

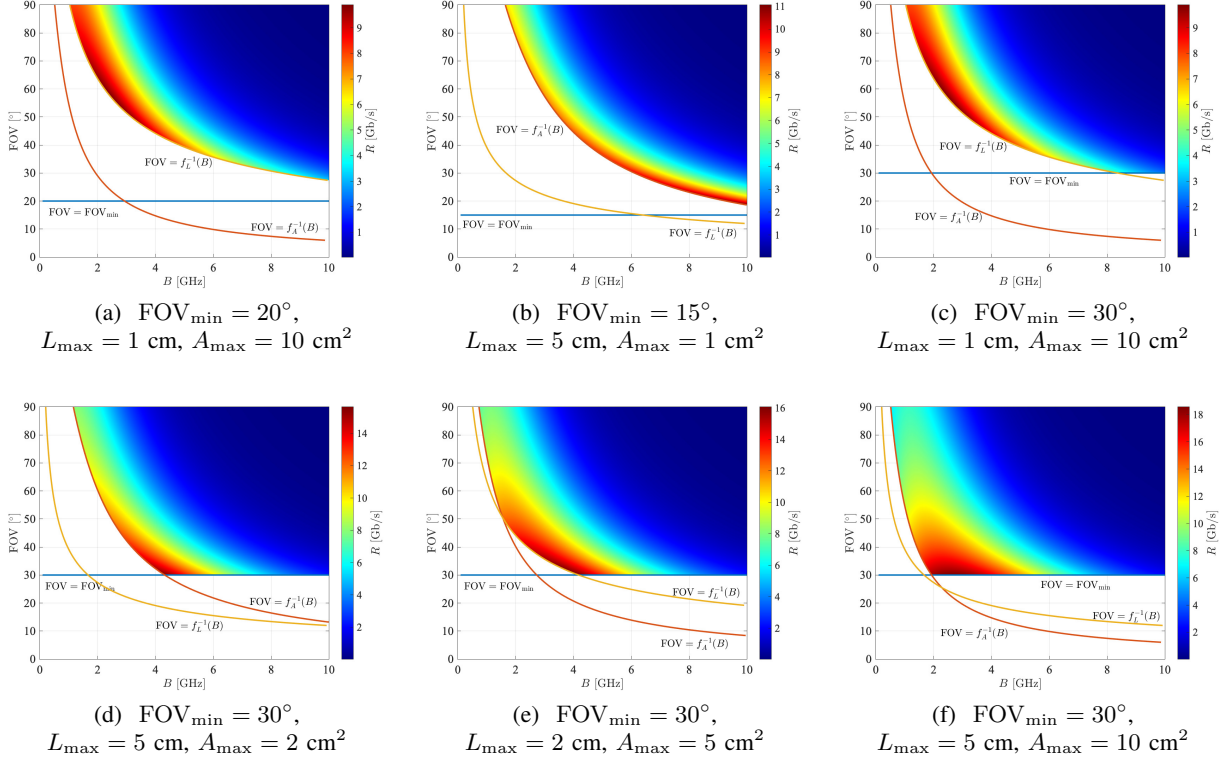


Fig. 9. Various realisations of the feasible region for the optimisation problem in (25) under Config. 2.

Therefore, in a multi-tier ADR, increasing the number of tiers allows the use of a smaller PD array size to meet the same data rate and FOV requirements.

C. Rate Maximisation Under Joint FOV and Overall Dimensions Constraints

Fig. 9 displays various realisations of the feasible region for the optimisation problem in (25). The feasible region on the B -FOV plane is the intersection of the overlapping areas formed by the three constraints in (25b), (25c) and (25d). The boundary of the area resulting from the constraint $A_{\text{ADR}} \leq A_{\max}$ is determined by the nonlinear function $\text{FOV} = f_A^{-1}(B)$ in (26). Similarly, the nonlinear function $\text{FOV} = f_L^{-1}(B)$ in (27) defines the boundary of the area due to the constraint $L_{\text{ADR}} \leq L_{\max}$. The boundary curves can have up to three intersection points within the range of interest and one or two of the boundary conditions can be dominant depending on the values of FOV_{\min} , A_{\max} and L_{\max} .

The examples provided in Fig. 9 represent six possible outcomes of the feasible region arising from different configurations of the constraints. In Figs. 9(a) and 9(b), two of the three constraints are inactive and one of them solely controls the feasible region. In Figs. 9(c) and 9(d), on the other hand, one of the constraints is inactive and the intersection of the other two constitutes the feasible region. Figs. 9(e) and 9(f) illustrate two more examples for the case where the constraints

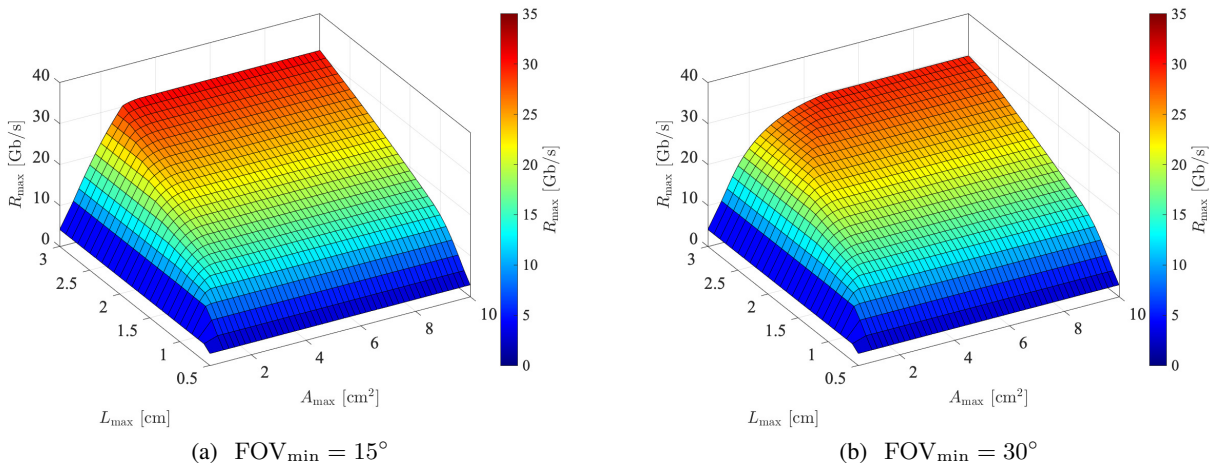


Fig. 10. The maximum achievable data rate R_{\max} as a function of the dimensions A_{\max} and L_{\max} for Config. 3 and $w_0 = 10 \mu\text{m}$.

intersect pairwise at three distinct points. In this case, all the three constraints actively participate in determining the feasible region. Note that there are other possible realisations for the feasible region that are not shown in Fig. 9. For instance, in each case, depending on how large FOV_{\min} is chosen, it may or may not cross the boundary curves of the other two constraints. Furthermore, it can be visually verified that the solution to the rate maximisation problem always lies on the boundary of the feasible region, as already anticipated by Lemma 3.

Fig. 10 shows the maximum achievable rate R_{\max} for Config. 3 with 8×8 PD arrays when L_{\max} and A_{\max} are variable, for two values of $\text{FOV}_{\min} = 15^\circ, 30^\circ$, assuming $w_0 = 10 \mu\text{m}$. This figure can be used to identify conditions under which one of the two constraints $L_{\text{ADR}} \leq L_{\max}$ or $A_{\text{ADR}} \leq A_{\max}$ becomes inactive; for instance, for a given $L_{\max} = \hat{L}$, there exists \hat{A} such that $A_{\text{ADR}} \leq A_{\max}$ is inactive for $A_{\max} \geq \hat{A}$. Based on Fig. 10(a), for $L_{\max} = 2 \text{ cm}$, the constraint on A_{ADR} turns out to be inactive for $A_{\max} \geq 2.5 \text{ cm}^2$, as R_{\max} is constant when $A_{\max} \geq 2.5 \text{ cm}^2$. In addition, it can be observed that R_{\max} is an increasing function of both A_{\max} and L_{\max} . For $\text{FOV}_{\min} = 15^\circ$, peak data rates greater than 25 Gb/s and up to 30 Gb/s are achieved at the cost of large ADR dimensions with $L_{\max} \geq 2.5 \text{ cm}$ and $A_{\max} \geq 3 \text{ cm}^2$. When FOV_{\min} goes up to 30° , R_{\max} does not exceed 30 Gb/s for $L_{\max} \geq 2.5 \text{ cm}$ and $A_{\max} \geq 4 \text{ cm}^2$.

VI. COMPACT ADR DESIGN USING CPC LENGTH TRUNCATION

Although CPCs are superior to other types of concentrators in terms of optical gain, the main drawback of CPCs lies in their relatively long length compared to the diameter of the collecting aperture. A practical and cost effective solution for reducing the length of CPCs is truncation [14], [15]. Length truncation slightly reduces the size of the entrance aperture. This effect has been investigated in detail for 2D and 3D CPCs in [16]–[18]. Since the parabolic surface of a

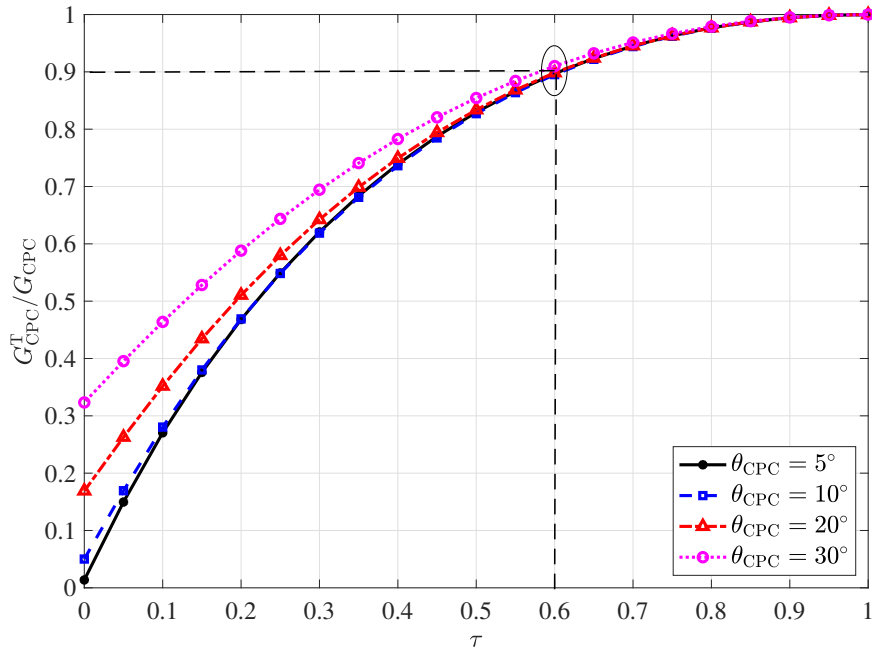


Fig. 11. The CPC concentration gain as a function of the truncation ratio τ for $n_{\text{CPC}} = 1.7$ and $D_2 = 1.5$ mm.

CPC near the entrance aperture is almost parallel to the optical axis, it can be truncated well short of the full CPC length without a significant reduction in the entrance aperture size. As a result, truncated CPCs exhibit a minor decrease in the concentration gain, and yet they reach a better optical efficiency because the light undergoes less number of internal reflections as compared to full-length CPCs.

A. Modified ADR Design Using Truncated CPCs

Let D_1^T , L_{CPC}^T , G_{CPC}^T and θ_{CPC}^T denote the diameter of the entrance aperture, the length, the concentration gain and the acceptance angle of a truncated CPC, while D_1 , L_{CPC} , G_{CPC} and θ_{CPC} are the respective parameters of a full-length CPC. The truncation ratio is denoted by τ so that $L_{\text{CPC}}^T = \tau L_{\text{CPC}}$ for $0 < \tau < 1$. Besides the length reduction, truncation rather increases the acceptance angle of a CPC, albeit its impact on the overall angular collection performance is insignificant. The findings in [17] have corroborated that $\theta_{\text{CPC}}^T \approx \theta_{\text{CPC}}$ is the case for $\tau \geq 0.5$. Fig. 11 shows the normalised concentration gain of a truncated CPC as a function of τ for different values of θ_{CPC} , assuming $n_{\text{CPC}} = 1.7$ and $D_2 = 1.5$ mm. It can be observed that the four characteristic curves are nearly overlapping for $\tau \geq 0.4$, for which $G_{\text{CPC}}^T \geq 0.9G_{\text{CPC}}$. Also, $G_{\text{CPC}}^T \approx 0.9G_{\text{CPC}}$ for $\tau = 0.6$ for all four values of θ_{CPC} , which means a 40% length reduction leads to only 10% gain loss. In the following, we use this as a simplifying assumption.

In this case, the problem statements in (23) and (25) can be modified by introducing appropriate

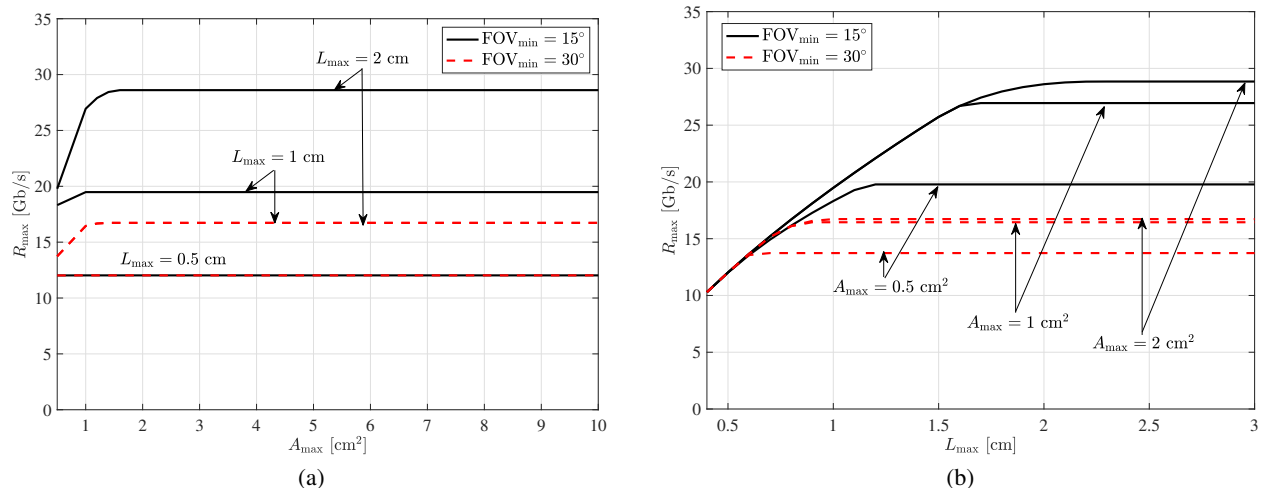


Fig. 12. The maximum achievable data rate R_{\max} as a function of (a) A_{\max} and (b) L_{\max} for Config. 1 with $\tau = 0.6$

coefficients into the ADR parameters. In particular, for the modified ADR, it suffices to replace D_1 and L_{CPC} by $D_1^{\text{T}} = \sqrt{0.9}D_1$ and $L_{\text{CPC}}^{\text{T}} = 0.6L_{\text{CPC}}$ through the use of (15) and (16). Denoting the total effective area and the overall height of this modified ADR by $A_{\text{ADR}}^{\text{T}}$ and $L_{\text{ADR}}^{\text{T}}$, respectively, $L_{\text{ADR}}^{\text{T}} \approx 0.6L_{\text{CPC}}$ and $A_{\text{ADR}}^{\text{T}} = 0.9A_{\text{ADR}}$ based on (17) and (18). Subsequently, the objective function in (23a) and (25a) is updated by recalculating the received power P_r in (19) for D_1^{T} . In addition, the constraints in (25c) and (25d) change to $L_{\text{ADR}}^{\text{T}} \leq L_{\max}$ and $A_{\text{ADR}}^{\text{T}} \leq A_{\max}$. Note that the FOV constraint in (23b) and (25b) does not change, since $\theta_{\text{CPC}}^{\text{T}} \approx \theta_{\text{CPC}}$. With these modifications, although the main parameters affected including D_1^{T} , $L_{\text{ADR}}^{\text{T}}$ and $A_{\text{ADR}}^{\text{T}}$ are involved in the achievable rate analysis, the essence of the rate maximisation problem is preserved. This means the same solutions already developed for the original problems in (23) and (25) by means of Theorem 1 and Theorem 2 would apply to the modified ADR optimisation problems. Now, let us proceed to the maximum achievable rate performance of the modified ADR design based on truncated CPCs with $\tau = 0.6$ as discussed.

B. Performance Evaluation

We consider the rate maximisation problem under joint FOV and overall dimensions constraints as outlined in (25). For a given set of the constrains, the resulting feasible region may fall within one of the various categories shown in Fig. 9. To shed light on the impact of each constraint on the maximum achievable data rate, Fig. 12 demonstrates R_{\max} for different values of the constraints, based on Config. 1 in Table II. In Fig. 12(a), R_{\max} is plotted against A_{\max} for $L_{\max} = 0.5, 1, 2$ cm and $\text{FOV}_{\min} = 15^\circ, 30^\circ$. It can be seen that in the case of $L_{\max} = 0.5$ cm, the change in FOV_{\min} does not make any difference in R_{\max} , since one of the dimensions constraints already dominates

the maximum rate performance. Specifically, $L \leq L_{\max}$ is the most restrictive constraint which limits the performance at $R_{\max} = 12$ Gb/s no matter how large A_{\max} is chosen. For both cases of $L_{\max} = 1, 2$ cm, on the other hand, the FOV constraint does have an influence on the performance in that R_{\max} improves by decreasing FOV_{\min} . For $L_{\max} = 1$ cm, the performance is limited at $R_{\max} = 17, 19.5$ Gb/s for $\text{FOV}_{\min} = 15^\circ, 30^\circ$, respectively, when $A_{\max} \geq 1$ cm². In the case of $L_{\max} = 2$ cm, R_{\max} reaches constant values of 17 Gb/s for $A_{\max} \geq 1$ cm² and 28.5 Gb/s for $A_{\max} \geq 1.5$ cm², corresponding to $\text{FOV}_{\min} = 15^\circ, 30^\circ$.

In Fig. 12(b), R_{\max} is evaluated as a function of L_{\max} for $A_{\max} = 0.5, 1, 2$ cm² and $\text{FOV}_{\min} = 15^\circ, 30^\circ$. For $A_{\max} = 1, 2$ cm², it is evident that the choice of FOV_{\min} has no effect on the maximum rate performance when $L_{\max} \leq 0.7$ cm. By decreasing A_{\max} to 0.5 cm², this is the case as long as $L_{\max} \leq 0.6$ cm. After L_{\max} exceeds these thresholds, R_{\max} varies with all three constraints. For sufficiently large values of L_{\max} , however, the rate maximisation is mainly controlled by the FOV constraint as well as the total effective area constraint. For $\text{FOV}_{\min} = 30^\circ$, the performance reaches no greater than $R_{\max} = 13.8, 16.8, 17$ Gb/s for $A_{\max} = 0.5, 1, 2$ cm², respectively. With $\text{FOV}_{\min} = 15^\circ$, these limits are improved to $R_{\max} = 20, 27, 29$ Gb/s at the cost of halving the minimum FOV. In this case, R_{\max} retains its growing trend with L_{\max} over a wider range of L_{\max} while approaching its upper limit. In fact, the constraint on FOV is relaxed enough allowing the two constraints on L_{ADR} and A_{ADR} to take control of the rate maximisation across the boundary of the feasible region.

Fig. 13 compares the modified ADR based on truncated CPCs versus the original ADR using full-length CPCs in terms of the maximum achievable rate performance. Recall that Configs. 1–3 represent a 1-tier ADR with 2×2 , 4×4 and 8×8 PD arrays, respectively, per receiver element. To make a fair comparison, we use the same set of FOV_{\min} , L_{\max} and A_{\max} for both ADR designs. Depending on the values of these parameters, three operating regimes are distinguished as no constraint on dimensions (NCD) as shown in Figs. 13(a) and 13(d), moderately constrained dimensions (MCD) as shown in Figs. 13(b) and 13(e), and strictly constrained dimensions (SCD) as shown in Figs. 13(c) and 13(f). When there is no constraint on dimensions, both ADR designs achieve almost the same performance and follow an identical decreasing trend with FOV_{\min} . In this case, the performance of the modified ADR is only slightly lower, which is attributed to the 10% loss in the optical gain of CPCs because of the 40% length truncation. Also, Configs. 1 and 3 mark the lowest and the highest performance levels, respectively. Notwithstanding, Configs. 1–3 attain $R_{\max} > 15$ Gb/s with $\text{FOV}_{\min} = 30^\circ$. The modified ADR design manifests its advantage when there are constraints on dimensions. Under MCD, for $L_{\max} = 2$ cm and $A_{\max} = 4$ cm², the modified ADR realises considerably higher performance bounds as compared to the original

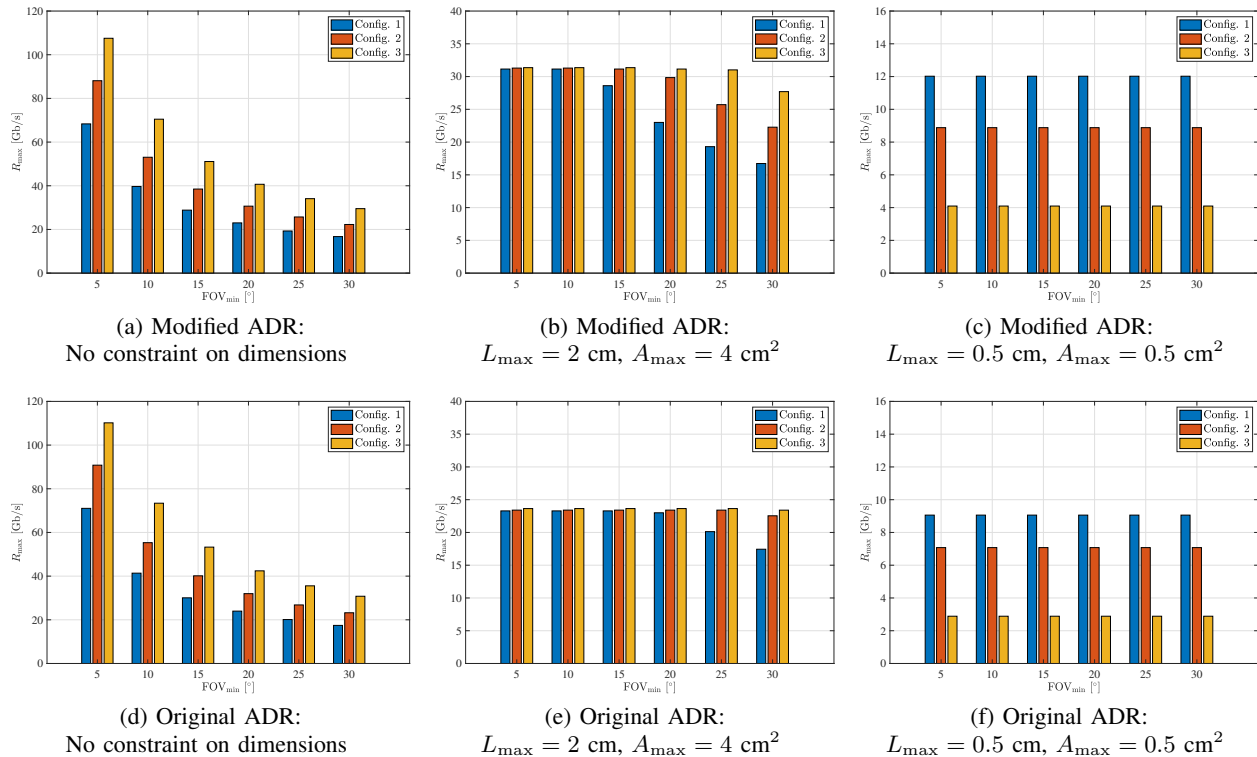


Fig. 13. The maximum achievable rate R_{\max} vs. FOV_{\min} for different PD array sizes and $w_0 = 10 \mu\text{m}$.

ADR. In the case of SCD, for $L_{\max} = 0.5 \text{ cm}$ and $A_{\max} = 0.5 \text{ cm}^2$, each configuration for each ADR design yields an equal performance level for all values of FOV_{\min} . It is noteworthy that, in contrast to NCD, the order of Configs. 1–3 in holding the lowest-to-highest performance levels is reversed under SCD. This indicates that under extremely limiting constraints on dimensions, increasing the PD array size in fact adversely affects the receiver performance. The modified ADR of $L_{\max} = 0.5 \text{ cm}$ and $A_{\max} = 0.5 \text{ cm}^2$ is a compact ADR design that achieves $R_{\max} = 12 \text{ Gb/s}$ with $\text{FOV}_{\min} = 30^\circ$ based on a 2×2 PD array. The highest performance achieved by the original ADR under the same conditions is just above 9 Gb/s .

VII. CONCLUSIONS

An in-depth study of the fundamental design tradeoffs was conducted for non-imaging ADRs based on CPCs. Building on a two-stage diversity combining scheme that reduces the complexity, a unified and tractable analytical framework was developed to meet the challenging requirements for high performance laser-based optical wireless receivers. A non-convex optimisation problem was formulated for maximising the achievable data rate R under constraints on FOV, the overall height L_{ADR} and the total top area A_{ADR} , to find optimum values of FOV and the PD bandwidth B for a given PD array size. First, with an objective to achieve $R \geq 10 \text{ Gb/s}$ under the minimum

FOV constraint only, the results evince a tradeoff between R and FOV. In particular, $R = 10$ Gb/s is realised with $\text{FOV} \leq 65^\circ$, while $R = 20$ Gb/s is achieved with $\text{FOV} \leq 28^\circ$. Alternatively, when FOV is fixed, R has an absolute maximum with respect to B , indicating that the performance is indeed degraded if the bandwidth is increased beyond a certain threshold. For $\text{FOV} = 30^\circ$, the peak data rates of $R = 14.00, 18.56, 24.53$ Gb/s are observed at $B = 2.1, 2.7, 3.5$ GHz for $2 \times 2, 4 \times 4$ and 8×8 PD arrays, respectively. Hence, when there is no constraint on the receiver dimensions, increasing the PD array size improves the maximum rate performance, even though a 2×2 PD array serves the purpose of fulfilling $R \geq 10$ Gb/s. For jointly satisfying $R \geq 10$ Gb/s and $\text{FOV} \geq 30^\circ$, the design space enlarges by increasing the PD array size used for each ADR element as well as by adding to the number of ADR tiers. It was shown that the design spaces provided by a 2-tier ADR with 4×4 PD arrays and a 3-tier ADR using 2×2 PD arrays are almost equally large.

In the presence of the constraints on dimensions, the results bring out an exacting tradeoff of practical importance for designing wide FOV ADRs: acquiring a small footprint and achieving a high data rate are opposing objectives. For a 1-tier ADR based on 8×8 PD arrays with $\text{FOV}_{\min} = 30^\circ$, $R_{\max} = 30$ Gb/s provided that $L_{\max} \geq 3$ cm and $A_{\max} \geq 4$ cm². The same ADR configuration reaches $R_{\max} = 10$ Gb/s if $L_{\max} = 1$ cm and $A_{\max} = 2$ cm². The results also demonstrate the significant impact of choosing small values for L_{\max} such that the overall height constraint takes over the performance when L_{\max} reduces to 0.5 cm. To overcome this challenge, a modified ADR solution by means of 40% length truncation for CPCs was proposed. It turns out that this truncation has only a marginal impact on the overall performance when the dimensions are unconstrained. The modified ADR has an advantage over the original ADR made of full-length CPCs under moderately to strictly constrained dimensions. It was found that under extremely limiting constraints on dimensions, the use of larger PD arrays significantly degrades the maximum achievable rate. However, with the proposed modification, a compact ADR design of $L_{\max} = 0.5$ cm and $A_{\max} = 0.5$ cm² is able to achieve $R_{\max} = 12$ Gb/s with $\text{FOV}_{\min} = 30^\circ$ based on a 2×2 PD array. Future research includes a comparison of imaging versus non-imaging receivers, and performance optimisation of multi-beam optical wireless networks by using ADRs with mobility and random orientation.

ACKNOWLEDGEMENT

The authors acknowledge financial support from the Engineering and Physical Sciences Research Council (EPSRC) under grant EP/S016570/1 ‘Terabit Bidirectional Multi-User Optical Wireless System (TOWS) for 6G LiFi’.

APPENDIX A
PROOF OF PROPOSITION 1

The partial derivative of R with respect to FOV is obtained by using (22):

$$\frac{\partial R}{\partial \text{FOV}} = \frac{2B}{\ln 2} \left(\frac{R_{\text{PD}}^2 P_r}{\Gamma N_0 B + R_{\text{PD}}^2 P_r^2} \right) \frac{\partial P_r}{\partial \text{FOV}}. \quad (33)$$

Based on (12) and (19), it follows that:

$$\frac{\partial P_r}{\partial \text{FOV}} = \left(\frac{1}{2N_{\text{tier}} + 1} \right) \frac{\partial P_r}{\partial \theta_{\text{CPC}}} = \left(\frac{1}{2N_{\text{tier}} + 1} \right) \frac{P_t D_1 \text{FF}}{(w'(D))^2} \exp \left(-\frac{D_1^2}{2(w'(D))^2} \right) \frac{\partial D_1}{\partial \theta_{\text{CPC}}}. \quad (34)$$

According to (33) and (34), the polarity of $\frac{\partial R}{\partial \text{FOV}}$ depends on the last product term, $\frac{\partial D_1}{\partial \theta_{\text{CPC}}}$. Based on (15), the partial derivative of D_1 with respect to θ_{CPC} is given by:

$$\frac{\partial D_1}{\partial \theta_{\text{CPC}}} = \frac{2K_1}{B} \left(-\frac{n_{\text{CPC}} \cos \theta_{\text{CPC}}}{\sin^2 \theta_{\text{CPC}}} \right) < 0, \quad (35)$$

because $\cos \theta_{\text{CPC}} > 0$ due to Corollary 1. As a result, $\frac{\partial R}{\partial \text{FOV}} < 0$, hence the proof is completed.

APPENDIX B
PROOF OF PROPOSITION 2

It is clear from (17) that $\frac{\partial L_{\text{ADR}}}{\partial B} < 0$. By using (12) and (17), the partial derivative of L_{ADR} with respect to FOV is derived in the form:

$$\begin{aligned} \frac{\partial L_{\text{ADR}}}{\partial \text{FOV}} &= \left(\frac{1}{2N_{\text{tier}} + 1} \right) \frac{\partial L_{\text{ADR}}}{\partial \theta_{\text{CPC}}} = \left(\frac{1}{2N_{\text{tier}} + 1} \right) \times \\ &\frac{K_1}{B} \left(-\frac{2n_{\text{CPC}} \sin \theta_{\text{CPC}} + n_{\text{CPC}} \sin \theta_{\text{CPC}} \tan^2 \theta_{\text{CPC}} + \tan^2 \theta_{\text{CPC}}}{\sin^2 \theta_{\text{CPC}} \tan^2 \theta_{\text{CPC}}} \right). \end{aligned} \quad (36)$$

Considering the fact that $\theta_{\text{CPC}} \leq \frac{\pi}{6}$ from Corollary 1, $\sin \theta_{\text{CPC}} > 0$. Consequently, $\frac{\partial L_{\text{ADR}}}{\partial \text{FOV}} < 0$.

Also, based on (18), it can be readily verified that $\frac{\partial A_{\text{ADR}}}{\partial B} < 0$. By using (12) and (18), the partial derivative of A_{ADR} with respect to FOV is obtained as follows:

$$\begin{aligned} \frac{\partial A_{\text{ADR}}}{\partial \text{FOV}} &= \left(\frac{1}{2N_{\text{tier}} + 1} \right) \times \\ &\frac{K_2}{B^2} \left[-\frac{2 \sin \theta_{\text{CPC}} \cos \theta_{\text{CPC}}}{\sin^4 \theta_{\text{CPC}}} \left(1 + \sum_{i=1}^{N_{\text{tier}}} 6i \cos(2i\theta_{\text{CPC}}) \right) - \frac{1}{\sin^2 \theta_{\text{CPC}}} \sum_{i=1}^{N_{\text{tier}}} 12i^2 \sin(2i\theta_{\text{CPC}}) \right]. \end{aligned} \quad (37)$$

Since $\theta_{\text{CPC}} \leq \frac{\pi}{6}$, $\sin \theta_{\text{CPC}} > 0$ and $\cos \theta_{\text{CPC}} > 0$. Also, $2i\theta_{\text{CPC}} < \frac{\pi}{2}$, thus $\sin(2i\theta_{\text{CPC}}) > 0$ and $\cos(2i\theta_{\text{CPC}}) > 0$. Therefore, $\frac{\partial A_{\text{ADR}}}{\partial \text{FOV}} < 0$. This completes the proof.

REFERENCES

- [1] E. Sarbazi, H. Kazemi, M. D. Soltani, M. Safari, and H. Haas, "Design Tradeoffs of Non-Imaging Angle Diversity Receivers for 6G Optical Wireless Access Networks," in *2022 IEEE Global Communications Conference (GLOBECOM)*, 2022.
- [2] M. Z. Chowdhury, M. Shahjalal, S. Ahmed, and Y. M. Jang, "6G Wireless Communication Systems: Applications, Requirements, Technologies, Challenges, and Research Directions," *IEEE Open Journal of the Communications Society*, vol. 1, pp. 957–975, 2020.
- [3] T. Koonen, K. Mekonnen, Z. Cao, F. Huijskens, N. Q. Pham, and E. Tangdiongga, "Ultra-High-Capacity Wireless Communication by Means of Steered Narrow Optical Beams," *Philosophical Transactions of the Royal Society A: Mathematical, Physical and Engineering Sciences*, vol. 378, no. 2169, p. 20190192, 2020.
- [4] H. Kazemi, E. Sarbazi, M. D. Soltani, M. Safari, and H. Haas, "A Tb/s Indoor Optical Wireless Backhaul System Using VCSEL Arrays," in *2020 IEEE 31st Annual International Symposium on Personal, Indoor and Mobile Radio Communications*, 2020, pp. 1–6.
- [5] E. Sarbazi, H. Kazemi, M. D. Soltani, M. Safari, and H. Haas, "A Tb/s Indoor Optical Wireless Access System Using VCSEL Arrays," in *2020 IEEE 31st Annual International Symposium on Personal, Indoor and Mobile Radio Communications*, 2020, pp. 1–6.
- [6] H. Kazemi, E. Sarbazi *et al.*, "A Tb/s Indoor MIMO Optical Wireless Backhaul System Using VCSEL Arrays," *IEEE Trans. Commun.*, vol. 70, no. 6, pp. 3995–4012, 2022.
- [7] S. B. Alexander, *Optical Communication Receiver Design*. Bellingham: SPIE Press, 1997.
- [8] S. D. Personick, "Receiver Design for Digital Fiber Optic Communication Systems," *Bell System Technical Journal*, vol. 52, no. 6, pp. 843–874, 1973.
- [9] J. M. Kahn and J. R. Barry, "Wireless Infrared Communications," *Proc. IEEE*, vol. 85, no. 2, pp. 265–298, Feb. 1997.
- [10] Y. Kaymak, R. Rojas-Cessa *et al.*, "A Survey on Acquisition, Tracking, and Pointing Mechanisms for Mobile Free-Space Optical Communications," *IEEE Communications Surveys & Tutorials*, vol. 20, no. 2, pp. 1104–1123, 2018.
- [11] M. M. Abadi, M. A. Cox *et al.*, "A Space Division Multiplexed Free-Space-Optical Communication System that Can Auto-Locate and Fully Self Align with a Remote Transceiver," *Scientific Reports*, vol. 9, no. 1, pp. 1–8, 2019.
- [12] M. A. Fernandes, B. T. Brandao *et al.*, "Adaptive Optical Beam Alignment and Link Protection Switching for 5G-Over-FSO," *Optics Express*, vol. 29, no. 13, pp. 20 136–20 149, 2021.
- [13] F. P. Guiomar, M. A. Fernandes *et al.*, "Coherent Free-Space Optical Communications: Opportunities and Challenges," *Journal of Lightwave Technology*, vol. 40, no. 10, pp. 3173–3186, 2022.
- [14] R. Winston, J. C. Minano, P. G. Benitez *et al.*, *Nonimaging Optics*. Elsevier, 2005.
- [15] D. Tsonev, "Concentrator Height Reduction," Patent GB2565201A, Feb. 2019.
- [16] R. Winston and H. Hinterberger, "Principles of Cylindrical Concentrators for Solar Energy," *Solar Energy*, vol. 17, no. 4, pp. 255–258, 1975.
- [17] A. Rabl, "Optical and Thermal Properties of Compound Parabolic Concentrators," *Solar energy*, vol. 18, no. 6, pp. 497–511, 1976.
- [18] W. T. Welford and R. Winston, "Optics of Nonimaging Concentrators. Light and Solar energy," 1978.
- [19] T. Koonen, K. Mekonnen *et al.*, "Novel Broadband OWC Receiver with Large Aperture and Wide Field-of-View," in *2020 European Conference on Optical Communications (ECOC)*, 2020, pp. 1–4.
- [20] T. Koonen, K. A. Mekonnen *et al.*, "Beam-Steered Optical Wireless Communication for Industry 4.0," *IEEE Journal of Selected Topics in Quantum Electronics*, vol. 27, no. 6, pp. 1–10, 2021.

- [21] T. Umezawa, T. Sakamoto *et al.*, “High Speed 2-D Photodetector Array for Space and Mode-Division Multiplexing Fiber Communications,” *Journal of Lightwave Technology*, vol. 36, no. 17, pp. 3684–3692, 2018.
- [22] T. Umezawa, A. Matsumoto *et al.*, “Large Submillimeter High-Speed Photodetector for Large Aperture FSO Receiver,” *IEEE Journal of Selected Topics in Quantum Electronics*, pp. 1–1, 2021.
- [23] S. Collins, D. C. O’Brien, and A. Watt, “High Gain, Wide Field of View Concentrator for Optical Communications,” *Opt. Lett.*, vol. 39, no. 7, pp. 1756–1759, Apr 2014.
- [24] P. P. Manousiadis, S. Rajbhandari *et al.*, “Wide Field-of-View Fluorescent Antenna for Visible Light Communications Beyond the étendue Limit,” *Optica*, vol. 3, no. 7, pp. 702–706, Jul 2016.
- [25] Y. Dong, M. Shi *et al.*, “Nanopatterned Luminescent Concentrators for Visible Light Communications,” *Optics express*, vol. 25, no. 18, pp. 21 926–21 934, 2017.
- [26] O. Alkhazragi, A. Trichili *et al.*, “Wide-Field-of-View Optical Detectors Using Fused Fiber-Optic Tapers,” *Opt. Lett.*, vol. 46, no. 8, pp. 1916–1919, Apr 2021.
- [27] B. S. Ooi, O. Alkhazragi, and A. Trichili, “Wide-Field-of-View Optical Detectors Based on Fused Fiber-Optic Tapers for High-Speed Optical Wireless Communication,” in *Mesophotonics: Physics and Systems at Mesoscale*, vol. 12152, 2022, p. 1215202.
- [28] N. Q. Pham, K. A. Mekonnen *et al.*, “Automatic Gbps Receiver for Mobile Device in Beam-Steered Infrared Light Communication System,” *Journal of Lightwave Technology*, vol. 40, no. 20, pp. 6852–6859, 2022.
- [29] M. D. Soltani, H. Kazemi *et al.*, “High-Speed Imaging Receiver Design for 6G Optical Wireless Communications: A Rate-FOV Trade-Off,” *To appear in IEEE Transactions on Communications*, 2022. [Online]. Available: <https://arxiv.org/abs/2205.05626>
- [30] “Unmounted Aspheric Lens:354140-B,” Thorlabs. [Online]. Available: https://www.thorlabs.com/newgrouppage9.cfm?objectgroup_id=3811
- [31] J. Carruther and J. M. Kahn, “Angle Diversity for Nondirected Wireless Infrared Communication,” *IEEE Transactions on Communications*, vol. 48, no. 6, pp. 960–969, 2000.
- [32] Z. Chen, N. Serafimovski, and H. Haas, “Angle Diversity for an Indoor Cellular Visible Light Communication System,” in *2014 IEEE 79th Vehicular Technology Conference (VTC Spring)*, 2014, pp. 1–5.
- [33] B. E. A. Saleh and M. C. Teich, *Fundamentals of Photonics*, 3rd ed. John Wiley & Sons, Inc., 2019, vol. Part I: Optics.
- [34] *Safety of Laser Products - Part 1: Equipment Classification, Requirements and User’s Guide*, International Electrotechnical Commission (IEC) 60825-1:2014 Std., Aug. 2014.
- [35] *Recommended Practice for Laser Safety Measurements for Hazard Evaluation*, American National Standards Institute (ANSI) Z136.4-2021 Std., 2021.
- [36] R. Henderson and K. Schulmeister, *Laser Safety*. CRC Press, 2003.
- [37] L. A. Coldren, S. W. Corzine, and M. L. Masanovic, *Diode Lasers and Photonic Integrated Circuits*, 2nd ed. John Wiley & Sons, Inc., 2012.